Available online at www.sciencedirect.com
ScienceDirect
Journal of Applied Geophysics 61 (2007) 16–38
JOURNAL OF APPLIED GEOPHYSICS
www.elsevier.com/locate/jappgeo

Characterization of an unstable rock mass based on borehole logs and diverse borehole radar data

Thomas Spillmann [a], Hansruedi Maurer [a], Heike Willenberg [b], Keith F. Evans [b], Björn Heincke [a], Alan G. Green [a,*]

[a] *Institute of Geophysics, Swiss Federal Institute of Technology, ETH-Hönggerberg, CH-8093, Zürich, Switzerland*
[b] *Geological Institute, Swiss Federal Institute of Technology, ETH-Hönggerberg, CH-8093, Zürich, Switzerland*

Received 13 October 2005; accepted 7 April 2006

Abstract

Unstable rocky slopes are major hazards to the growing number of people that live and travel though mountainous regions. To construct effective barriers to falling rock, it is necessary to know the positions, dimensions and shapes of structures along which failure may occur. To investigate an unstable mountain slope distinguished by numerous open fracture zones, we have taken advantage of three moderately deep (51.0–120.8 m) boreholes to acquire geophysical logs and record single-hole radar, vertical radar profiling (VRP) and crosshole radar data. We observed spallation zones, displacements and borehole radar velocity and amplitude anomalies at 16 of the 46 discontinuities identified in the borehole optical televiewer images. The results of the VRP and crosshole experiments were disappointing at our study site; the source of only one VRP reflection was determined and the crosshole velocity and amplitude tomograms were remarkably featureless. In contrast, much useful structural information was provided by the single-hole radar experiments. Radar reflections were recorded from many surface and borehole fracture zones, demonstrating that the strong electrical property contrasts of these features extended some distance into the adjacent rock mass. The single-hole radar data suggested possible connections between 6 surface and 4 borehole fractures and led to the discovery of 5 additional near-surface fracture zones. Of particular importance, they supplied key details on the subsurface geometries and minimum subsurface lengths of 8 of the 10 previously known surface fracture zones and all of the newly discovered ones. The vast majority of surface fracture zones extended at least 40–60 m into the subsurface, demonstrating that their depth and surface dimensions are comparable.

Keywords: Fracture mapping; Borehole geophysics; Vertical radar profiling (VRP); Crosshole radar; Single-hole radar

1. Introduction

Characterizing unstable rock slopes is an increasingly important task in mountainous regions worldwide. Significant expansions of population centres and transport routes in mountain valleys and exceptional climatic events related to global warming are amplifying the risk of catastrophic rock-slope failures (Bader and Kunz, 2000). To prevent loss of life and expensive infrastructure, appropriate mitigation measures in the form of early warning systems and protective barriers need to be implemented. For the construction of effective barriers, knowledge of the locations, sizes and geometries of brittle discontinuities that are the sources of rock-slope instabilities is required.

* Corresponding author. Tel.: +41 1 633 2657; fax: +41 1 633 1065.
E-mail address: alan@aug.ig.erdw.ethz.ch (A.G. Green).

0926-9851/$ - see front matter © 2006 Elsevier B.V. All rights reserved.
doi:10.1016/j.jappgeo.2006.04.006

Traditional approaches of investigating unstable mountain slopes include geological mapping, remote sensing, analyses of borehole logs and strain measurements at the surface and in boreholes (Cooke and Doornkamp, 1990; Erismann and Abele, 2001; Glade et al., 2005). Since these approaches only provide limited information on the depth distribution of geological structures, a variety of surface-based geophysical techniques have recently been employed in landslide and rockfall studies (McCann and Forster, 1990; Hack, 2000). Various combinations of ground-penetrating radar (georadar), seismic reflection, seismic refraction, electrical resistivity, self-potential and electromagnetic methods have been used to determine the geometries of failure planes and volumes of unstable rock (Bruno and Marillier, 2000; Cummings, 2000; Havenith et al., 2000; Jongmans et al., 2000; Schmutz et al., 2000; Dussauge-Peisser et al., 2003). In areas of crystalline rock distinguished by ubiquitous fractures and faults, the high-resolution capabilities of surface-based georadar methods have proven to be particularly useful. For example, Grasmueck (1996) and Heincke et al. (2005) have shown how three-dimensional (3-D) georadar mapping is capable of providing high-resolution images of shallow- to moderate-dipping fractures and brittle faults.

Unfortunately, surface-based georadar methods have limited depth penetration in areas covered by fine-grained sediments and they are not well suited for the reflection imaging of steeply dipping features, primarily because of the unfavourable radiation patterns of typical antennas (Engheta et al., 1982). This latter point is a fundamental shortcoming, because it is the steeply dipping fractures and faults that define the instability of many rocky mountain slopes.

To address the issue of probing deeper and mapping steeply dipping brittle discontinuities within unstable rock masses, we have investigated the utility of the single-hole radar reflection, vertical radar profiling (VRP) and crosshole radar techniques at an unstable mountain site in southern Switzerland. Individual and combined interpretations of the different radar data sets were constrained by the results of surface geological mapping and information supplied by geophysical borehole logs.

After a brief introduction to the study site and borehole radar techniques, we describe our borehole logging and radar data acquisition and processing procedures. We then present individual and combined interpretations of the processed data sets. Although all three types of borehole data furnish new information on subsurface features, the most important details are supplied by the single-hole radar reflection data. When constrained by complementary geological and geophysical information, these data yield high-resolution images of numerous steeply dipping fracture zones.[1]

2. Randa study site

2.1. The 1991 Randa rockslides

The area of interest lies immediately above a scarp created by the largest mass movement of rock in recent Swiss history. During the Spring of 1991, two major rockslides resulted in the release of 30 million m^3 of crystalline rock and the formation of a debris cone that obliterated holiday apartments and barns close to the village of Randa (Fig. 1) and blocked the main transport route connecting the Rhône valley to the main tourist resort of Zermatt (Schindler et al., 1993; Sartori et al., 2003). The debris cone dammed the Mattervispa River, causing flooding in upstream regions of the valley.

2.2. Continued instability

Various estimates based on geodetic measurements suggest that 2.7–9.2 million m^3 of the remaining mountain slope have been moving 0.01–0.02 m/year southeastwards since the 1991 rockslides (Eberhardt et al., 2001; Jaboyedoff et al., 2004; Willenberg, 2004). Movements have been concentrated across major fracture zones with opening rates of 0.001–0.003 m/year (Willenberg, 2004). Many of these brittle discontinuities occur within or close to our study site (Fig. 2). The continued instability of the mountain slope at Randa is a concern for the local population and responsible authorities.

2.3. Topographic relief, rock lithologies and fracture/fault distribution

The 140 × 143 m study site is located above the tree line at elevations of 2310–2400 m (Fig. 1b). Although the topography is extremely rugged (i.e. >90 m of elevation variation over the site), there are several relatively flat terraces (Figs. 2 and 3a).

Information on the geology in this region is based on rock exposures, geophysical logs recorded in three boreholes and analyses of aerial photographs (Willenberg,

[1] Since differential motion has occurred across many of the brittle discontinuities at our study site, they are faults. However, for simplicity we will refer to all brittle discontinuities as fracture zones in this contribution.

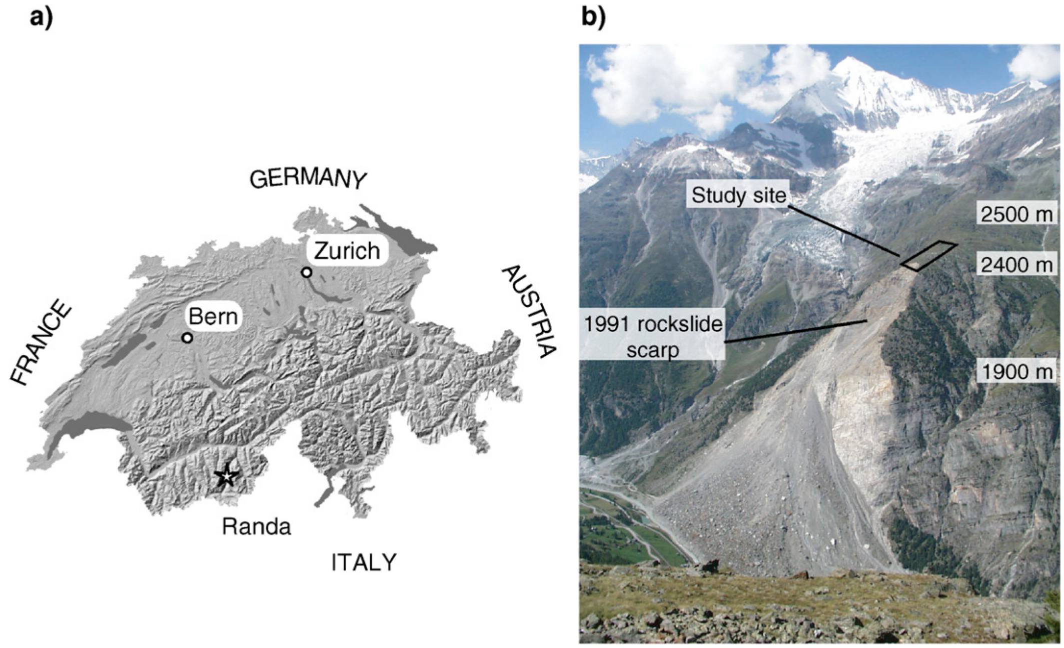

Fig. 1. a) Randa rockslide location (star) in the Matter Valley of southern Switzerland. b) Photograph of the Randa rockslide and study site. (Photo: H. Willenberg).

2004). The upper volume of the rock mass is dominated by heterogeneous gneisses with a strong 20–25° west–southwest-dipping foliation and three major fracture/fault systems F1–F3. The F1 system of fracture zones and ductile faults dips at shallow angles to the southwest, parallel to the strong bedrock foliation, whereas the other two systems comprise fracture zones that are mostly steeply dipping. On average, fractures of the F2 system strike between northeast–southwest and northwest–southeast with northwest to northeast dips (Z1 and Z6–Z10 in Fig. 2b), respectively, whereas those of the F3 system strike approximately north–south with easterly dips (Z2–Z5 in Fig. 2b). It is the steeply dipping fracture zones, some of which have openings of ten's of centimetres, that mostly influence the instability of the Randa mountain slope (Willenberg, 2004).

Photographs in Fig. 3b–d provide overviews of three open fracture zones. They range from jagged (Fig. 3b) to planar (Fig. 3c) and from closed (Fig. 3c) to open (Fig. 3d). At a number of locations, the fracture zones are buried beneath moraine and slope debris (maximum thickness of a few meters) covered by pasture and low-lying vegetation (Fig. 3a). In these regions, their interpolated or extrapolated positions are based on lineaments identified on aerial photographs. Fracture zones observed in outcrop or interpolated/extrapolated beneath the cover material are referred to as surface fracture zones in this contribution.

2.4. Boreholes

In an attempt to improve our understanding of failure mechanisms in massive crystalline rock, the unstable mountain slope at Randa has been subjected to a variety of geological, geotechnical and geophysical investigations (Eberhardt et al., 2001; Willenberg et al., 2004; Willenberg, 2004; Heincke et al., 2005, 2006, in press) Three moderately deep boreholes (SB120, SB50S and SB50N) were drilled through two of the flat terraces (Fig. 2). Borehole SB120 was 120.8 m deep and vertical until about 40 m depth. Thereafter, it deviated to the east so that the hole bottom lay 18 m to the east of the wellhead. In contrast, the 52.5 and 51.0 m deep boreholes SB50S and SB50N were approximately vertical, with maximum horizontal deviations of ~2 m. In many of the figures and the following text (unless stated otherwise), depths are given relative to a horizontal datum defined to be the top of borehole SB50N (2360.4 m above sea level).

3. Borehole radar methods

3.1. Single-hole radar

To record single-hole full-waveform radar data, a fixed-offset transmitter–receiver antenna pair is pulled slowly up the length of a borehole. Such data supply

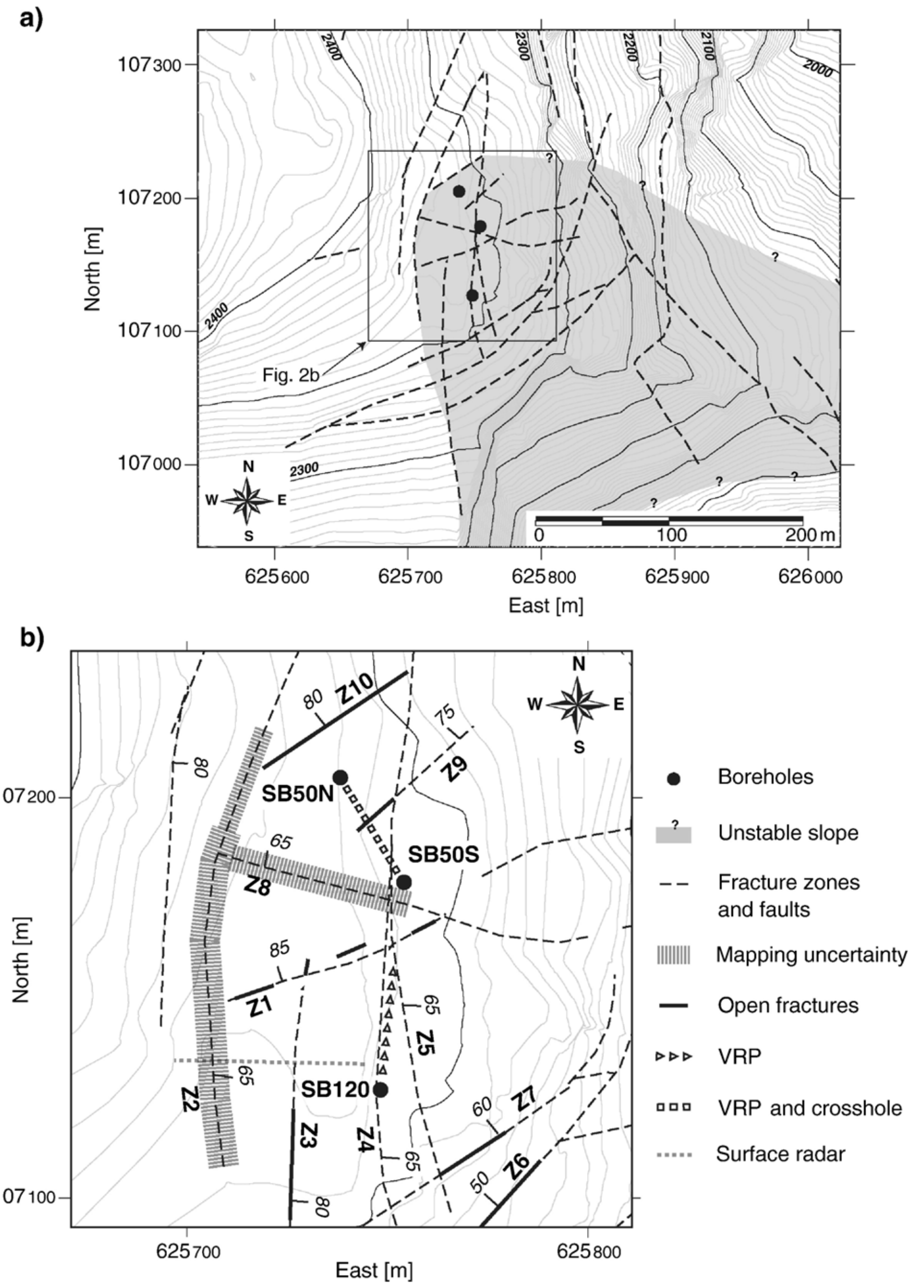

Fig. 2. a) Map of Randa study site (black frame in Fig. 1b) showing the extent of unstable rock based on geodetic measurements, the boreholes and major fracture zones. b) Enlargement of area surrounding the boreholes identifying the fracture zones and locations of the vertical radar profiles and crosshole radar plane. Hatching outlines zones of dislocation that are broad and/or hidden beneath a thin veneer of surficial material. Thick solid lines delineate open portions of fracture zones. Ticks and numbers identify the surface dip azimuth and dip.

information on the velocity and attenuation of radar waves in the vicinity of the borehole and on the nature of reflectors distributed about the borehole (Olsson et al., 1992; Wänstedt et al., 2000; Seol et al., 2004). The principle of the single-hole reflection method is similar to that of the surface-based georadar technique, except that reflectors may occur on all sides of the borehole recording line (Fig. 4). Planar features intersected by a borehole will appear as V-shaped reflections on a single-hole radar section. Because there is a finite separation between the transmitter and receiver antennas, reflections near the intersections of the two arms of the V's

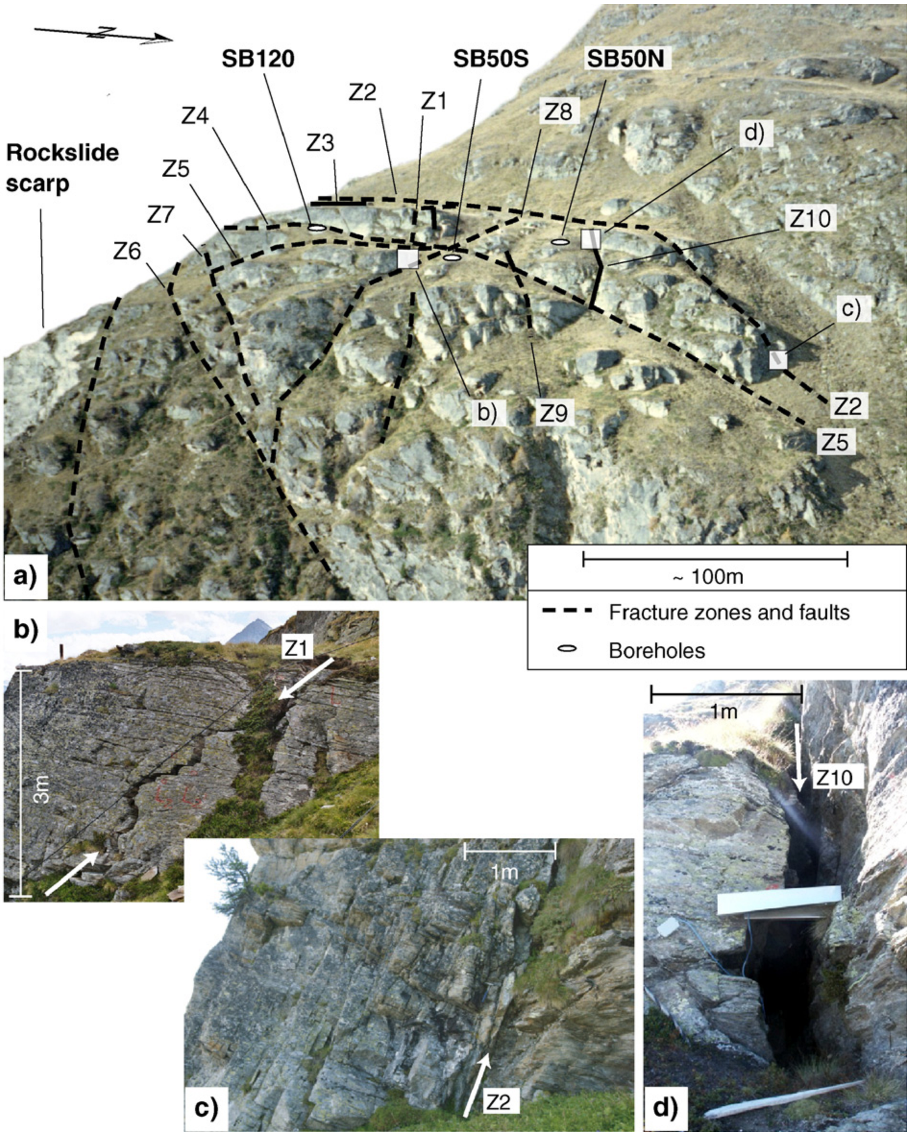

Fig. 3. a) Perspective view showing the moraine and slope debris covering part of the study site and the ruggedness of the terrain. Locations of photographs displayed in b)–d) are marked by white rectangles. Side views of b) a jagged portion of open fracture Z1, c) fracture zone Z2 and d) open fracture Z10. (Photos: B. Rinderknecht, H. Willenberg and E. Eberhardt).

will be hyperbolic shaped and no reflections will be recorded at the apices of the V's (i.e. along the axis of the recording system), where the antennas are located on opposite sides of the intersecting features.

Compared to surface-based georadar data, recordings in near-vertical boreholes are well suited for detecting steeply dipping features that are located more than a wavelength from the borehole, but not subhorizontal ones (Wänstedt et al., 2000). Due to the rotational symmetry of non-directional antennas operating in straight boreholes, the georadar data on their own do not provide sufficient information to determine unambiguously the locations of reflectors not intersected by the boreholes. To compensate for this limitation, constraints from other observations are necessary.

3.2. Vertical radar profiling (VRP)

Vertical radar profiling (VRP), the electromagnetic wave equivalent of the well know vertical seismic profiling (VSP) technique (Hardage, 1983; Dillon and Thomson, 1984), involves transmitting radar signals from multiple locations along lines at the surface to multiple locations in a borehole, or vice versa (Zhou and

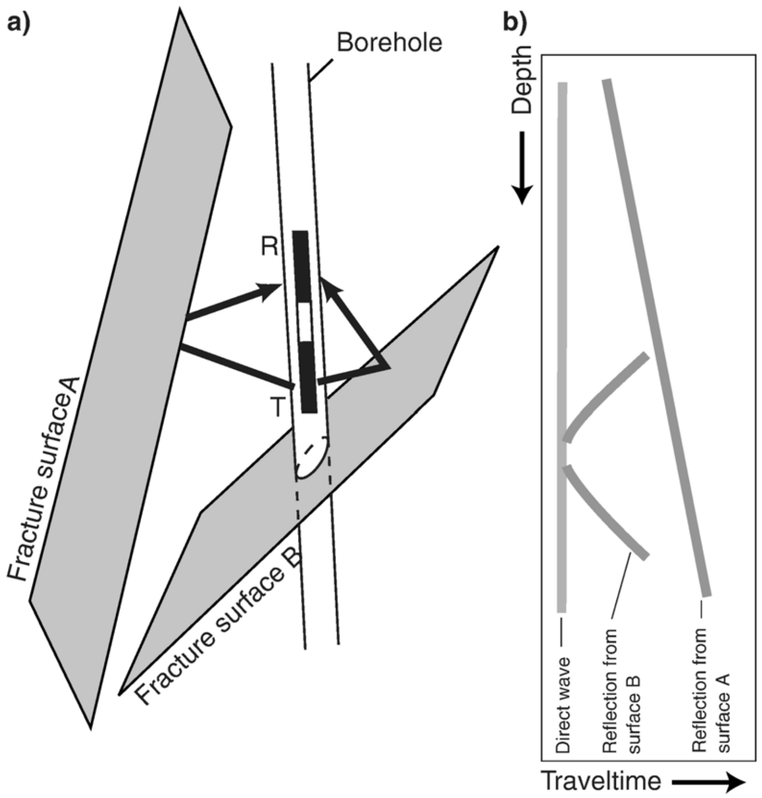

Fig. 4. a) Principle of single-hole reflection method and b) schematic reflection section illustrating typical reflection patterns from intersecting and non-intersecting fractures.

Sato, 2000; Tronicke and Knoll, 2005). As for the single-hole radar method, both the transmitted and reflected arrivals provide useful information and there may be ambiguities in reflector locations. The presence of a thick layer of electrically conductive sediments at the surface may preclude the use of the VRP technique and low amplitude signals will be recorded for certain locations and orientations of the receiver antenna relative to the transmitter antenna (Tronicke and Knoll, 2005).

3.3. Crosshole radar

By transmitting radar signals from one borehole to another, radar velocities and attenuation between the two boreholes can be estimated (e.g. Olsson et al., 1992; Wänstedt et al., 2000; Washbourne et al., 2002). For optimum illumination of target structures, the lengths of the boreholes used for a crosshole survey should be substantially greater than the borehole separation. Nevertheless, it is generally difficult to map thin elongated structures that parallel the boreholes (Menke, 1984; Rector and Washbourne, 1994).

4. Data acquisition

Drilling of boreholes at the Randa study site required a substantial logistical effort. Approximately 30 tons of equipment had to be transported by helicopter to the high mountain slope. Since the holes were percussion drilled, no cores were available. Steel casing was installed in the top 5 m of the three holes, which were dry except for the lower 10 m of SB120.

Table 1 provides an overview of parameters used for the geophysical logging and radar surveying; note, that depth information in this table is relative to the top of the respective boreholes. Lithological and structural information were determined from optical televiewer logs (column a in Figs. 5–7) and caliper logs (column f in Figs. 5–7). To derive horizontal displacements across active fracture zones, inclinometer casings grouted into the boreholes after completion of the geophysical measurements were resurveyed twice per year using a 0.61 m long inclinometer probe (column g in Figs. 5–7).

A MALA system with 100 MHz borehole and surface antennas was used to acquire all radar data. Single-hole

Table 1
Acquisition parameters used for borehole logging and georadar measurements at the Randa study site

	SB120	SB50S	SB50N
Borehole length	120.8 m	52.5 m	51.0 m
Optical televiewer			
Depth range	5.0–112.3 m	5.0–50.1 m	5.0–49.9 m
Four-arm caliper			
Depth range	5.0–120.0 m	5.0–52.0 m	5.0–50.6 m
Increment	0.01 m	0.01 m	0.01 m
Inclinometer			
Midpoint depth range	5.0–113.3 m	5.0–43.4 m	5.0–35.2 m
Increment	0.61 m	0.61 m	0.61 m
Vertical radar profile (VRP)			
Profile azimuth	6°	328°	148°
Surface offset range	0.5–28.5 m	0.5–30.5 m	0.0–24.0 m
Antenna depth range	5.2–50.7 m	5.2–51.2 m	5.2–49.7 m
Antenna increment	0.5 m	0.5 m	0.5 m
Single-hole radar			
Midpoint depth range	5.5–118.0 m	5.0–50.2	5.4–48.8 m
Increment	0.2 m	0.1 m	0.2 m
Crosshole radar		transmitter	receiver
Antenna depth range		5.2–51.2 m	5.2–49.7 m
Increment		0.5 m	0.5 m
Sonic			
Midpoint depth range		5.0–38.1 m	5.0–32.6 m
Increment		0.05 m	0.05 m

Depths in this table are relative to the top of the respective boreholes.

full-waveform data were recorded in all three holes at 0.1 or 0.2 m increments using transmitter and receiver antennas separated by 2.75 m. Three VRP's were collected along two surface lines. For one VRP, antennas were deployed in SB120 and along a roughly north-south line and for the other VRP's, antennas were deployed in SB50S and SB50N and along a line connecting the two boreholes (Fig. 2b). The antenna increment was 0.5 m and the surface antenna was oriented perpendicular to the surface lines (Tronicke and Knoll, 2005). Crosshole radar signals with sufficient signal-to-noise ratios could only be transmitted between SB50S and SB50N. Using an antenna increment of 0.5 m, signals from 93 transmitter positions were registered at 90 receiver positions.

Shortly after the radar surveys, the boreholes were cased with PVC tubes. This allowed SB50S and SB50N to be filled with water, thus facilitating the sonic logging. Installation of induction rings on the SB120 casing for vertical extension measurements resulted in a diameter that was too small to allow the sonic sonde to be used along the length of this hole. The SB50S and SB50N sonic logs were acquired using a borehole-compensated tool with a source frequency of 23 kHz and receivers located 0.71 and 1.11 m from the source. Full-waveforms were recorded every 0.05 m.

5. Radar and sonic log data processing

5.1. Single-hole radar

Based on their traveltimes and numerical modelling, the first detected arrivals in the single-hole radar data represent waves that travel through the rock (the amplitudes of the airwaves travelling along the borehole are too small to be detected). Correlation of these arrivals provide time lags that are converted to velocities representing the volumes of rock within 0.5–1.0 m of the boreholes (column j in Figs. 5–7). We estimate that the correlation process results in traveltime uncertainties of approximately ±0.5 ns, which translates to a velocity uncertainty of ±2.5% or ±0.003 m/ns for the Randa data; based on the results of the three types of radar survey, a representative velocity for the Randa rock mass is taken to be 0.120 m/ns. The absolute value of the first arriving pulses, be they negative or positive, provide the corresponding amplitude information (column k in Figs. 5–7).

To enhance the coherency of reflections, a relatively standard processing scheme was applied to the single-hole radar data. After aligning the first arriving pulses to compensate for near-borehole velocity heterogeneities, the data were amplitude scaled (i.e. trace equalisation using a narrow window centred on the first arrivals followed by multiplication of each trace value by t^2, where t is time), bandpass filtered (30–60 to 200–300 MHz) and FX deconvolved (Fig. 8a, d and g). To aid the interpretation, automatic-gain controlled (150 ns window) versions of the data were phase-shift migrated (Fig. 8c, f and i). Conventional migration is a valid processing step for the nearly vertical boreholes SB50S and SB50N and for the upper vertical part (~40 m) of SB120. It will produce only approximate or erroneous results for the lower curved part.

5.2. Vertical radar profiling (VRP)

Georadar velocities in the vicinity of the boreholes were derived from the VRP data. From the SB120, SB50S and SB50N data sets, we were able to pick 2439, 1445 and 1016 first arrival traveltimes with a picking uncertainty of ±2.0 ns. Inversions of these traveltimes provided velocity–depth models for the planes containing the boreholes and the surface recording lines (column i in Figs. 5–7).

Processing of the VRP reflection data included amplitude scaling (as for the single-hole radar data), bandpass filtering (30–60 to 150–230 MHz) and median filtering (3 samples, 11 traces) to minimize the effects of the direct arrivals. Examples of the only extensive reflections identified as originating from a common boundary at the Randa study site are outlined by red lines on the SB120 transmitter gathers displayed in Fig. 9. Numerous other reflections and diffractions in the Randa VRP data were either too limited in extent or observed on too few transmitter and receiver gathers to be located (see below and Appendices A and B). For the SB120 VRP data, transmitter positions extended to a maximum distance of 28.5 m and receivers were lowered to a maximum depth of 50.5 m relative to the top of the borehole (Table 1). From these data, a total of 1608 reflection times (event highlighted in Fig. 9) could be picked with an average picking uncertainty of ±5 ns.

Techniques developed for vertical seismic profiling data are intended primarily for mapping shallow- to moderate-dipping sedimentary units (Hardage, 1983; Dillon and Thomson, 1984). Since a preliminary analysis suggested that the identified reflections in Fig. 9 originated from a steeply dipping planar structure, it was necessary to develop an alternative approach (Fig. 10 and Appendix A). Given sources s_i ($i=1$ … number of source positions) along a surface profile and receivers r_j ($j=1$ … number of receiver positions) within a borehole, the goal is to estimate the position of planar feature P that is the origin of reflections with observed traveltimes t_{ij}. The position of P can be represented by a vector $\mathbf{p}_n$ that originates from an arbitrary origin and is perpendicular to P. The parameters defining $\mathbf{p}_n$ can be estimated using a brute force grid search approach, in which a trial vector $\mathbf{p}_n^{\text{trial}}$ is systematically varied in an attempt to determine the minimum root–mean square (RMS) difference between the observed reflection times and those predicted by $\mathbf{p}_n^{\text{trial}}$. Using a homogeneous velocity model, the predicted reflection times t_{ij}^{trial} can be calculated rapidly using the mirror source $\bar{s}_i$:

$$t_{ij}^{\text{trial}} = \frac{|\bar{s}_i - r_j|}{v}, \tag{1}$$

where v is the georadar propagation velocity and $|\bar{s}_i - r_j|$ is the distance between $\bar{s}_i$ and r_j (see Fig. 10). The results of applying our grid search algorithm to four synthetic reflectors with different orientations are shown in Appendix A. Given a suite of reflection traveltimes t_{ij}^{trial}, these tests demonstrate that there are generally two equally plausible solutions for $\mathbf{p}_n$.

Application of the grid search algorithm to the SB120 VRP data set (Appendix B) demonstrates that two planar reflectors with the following parameters can explain the picked reflection traveltimes with RMS differences of 3–4 ns: (1) surface distance to the top of SB120 = 23.6 ± 1.0 m, dip azimuth = 86 ± 8°, dip = 82 ± 4°, (2) surface distance to the top of SB120 = 22.0 ± 1.0 m, dip azimuth = 284 ± 8°, dip = 88 ± 4°. The parameters of reflecting plane (1) correspond closely to those of surface fracture zone Z3 (Fig. 2b): surface distance to the top of SB120 = 22 m, dip azimuth = 93°, dip = 80°. No surface features correlate with the reflecting plane (2). Consequently, our preferred solution is reflecting plane (1).

5.3. Crosshole radar

From the 93 × 90 crosshole radar traces acquired from boreholes SB50S and SB50N, we were able to measure the traveltimes and amplitudes of 7066 first-arrival pulses. The average picking uncertainty of the traveltimes was ∼2 ns. A non-linear tomographic scheme was employed for the inversion of the traveltimes (Musil et al., 2006). It included a finite-difference Eikonal solver for computing traveltimes and wave paths (Podvin and Lecomte, 1991) and a fat-ray method that accounts for the finite bandwidth of the data in calculating the sensitivities (Husen and Kissling, 2001). The zero times of the transmitted signals were refined during the inversion process using the procedure outlined by Maurer (1996).

After 10 iterations of the inversion scheme that was controlled 6% by the damping, 31% by the smoothing and 63% by the data, the velocity tomogram shown in Fig. 11a was obtained. The RMS difference between the observed traveltimes and those predicted by the final model was 0.7 ns, well below the estimated picking accuracy. Standard ray-based inversion of the amplitude data (Holliger et al., 2001; Musil et al., 2006) was performed using the radiation pattern of an infinitesimal vertical electric dipole and the ray paths obtained from the traveltime inversion. The resultant attenuation tomogram is presented in Fig. 11b.

5.4. Sonic logs

Arrival times of the P-wave onsets were picked manually from the full-waveform sonic data. Uncertainties

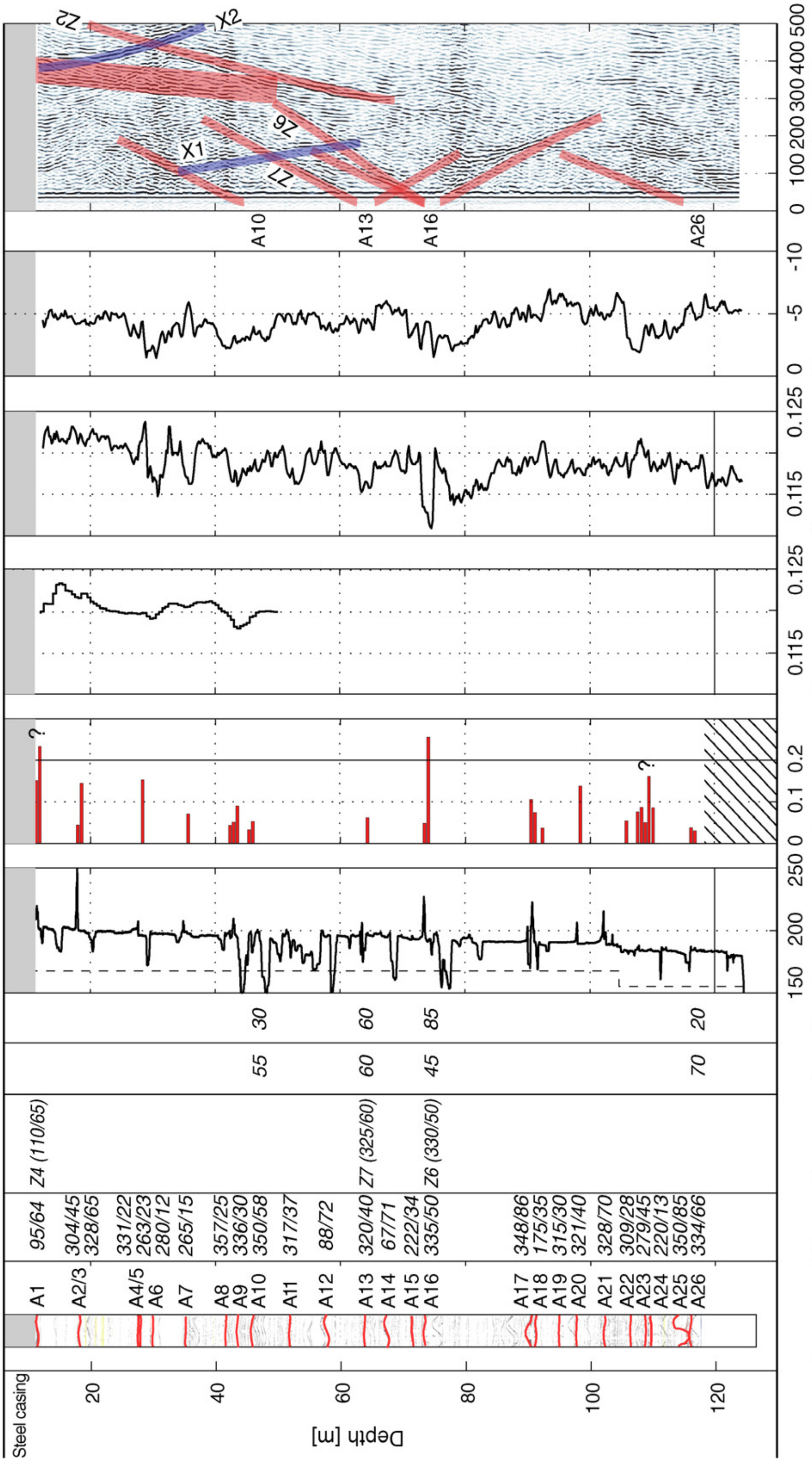
SB120
Steel casing
Depth [m]
a) Televiewer
b) Dip azimuth° / Dip°
c) Surface feature (Dip azimuth° / Dip°)
d) Radar reflection Dip°
e) Min. feature length [m]
f) Caliper area [cm2]
g) Dislocation velocity [cm/y]
i) VRP velocities [m/ns]
j) Single-hole radar velocities [m/ns]
k) Single-hole radar amplitudes [x10^3]
l) Single-hole radar reflection section
Time [ns]
Z4 (110/65)
Z7 (325/60)
Z6 (330/50)
X1
X2
Z2
Z6
Z7
A10
A13
A16
A26

in the traveltime differences between the two receivers were roughly 4 μs, which translated to a velocity uncertainty of approximately ±4% or ±0.2 km/s for the Randa data. The resulting velocity–depth functions were smoothed using a three-point median filter (column h in Figs. 6 and 7).

6. Results and interpretation

Considering the limited depth information available from surface observations, the local nature of the borehole logs and the ambiguities associated with the various georadar data sets, an integrated interpretation of all relevant details is necessary to estimate the depth distribution of fracture zones at the Randa study site. Even though fracture zones are observed at a large number of outcrops, substantial portions of these features are buried beneath thin layers of surficial material (Fig. 3a). As a consequence, our knowledge of the continuity and size of fracture zones shown in Fig. 2 is incomplete and other major brittle discontinuities may be hidden beneath the surficial cover. After describing the essential characteristics of the borehole logs, crosshole radar tomograms, VRP velocity–depth profiles and single-hole radar reflection sections, we use this information to determine the minimum depth extents of many fracture zones observed at the surface and within the boreholes and reveal the existence of major brittle discontinuities that have not been previously identified.

6.1. Borehole logs

Optical televiewer logs supply detailed information on the fractures intersected by the three boreholes. Discontinuities that have thicknesses of ≥2 mm and are either open or contain phyllonitic infill are highlighted by red lines in column a of Figs. 5–7. Repeated inclinometer measurements demonstrate that many of these are moving (column g in Figs. 5–7). Nevertheless, except for two or three examples, it is not obvious from the televiewer logs which of these fractures are major features that connect to the surface-mapped fracture zones (Figs. 2 and 3) or are examples of equally important hidden discontinuities. Furthermore, the azimuths and dips of discontinuities inferred from their expressions at the borehole walls may not be representative of their large-scale orientations.

The cross-sectional areas of the boreholes recorded in the caliper logs are significantly larger than those of the drill bits, with a tendency to decrease slightly with depth in SB120 and SB50 (column f in Figs. 5 and 6). These facets are consequences of the percussive drilling method used. There are also numerous anomalous increases and decreases in hole size, many of which correlate with the fracture zones. Hole enlargements can be explained by spalling of weak material around the discontinuities. Zones of spallation are particularly evident at the active fracture zones A2–A3, A16 and A17–A18 in SB120, S2–S8 in SB50S and N1–N2 and N7–N8 in SB50N. At several locations in all boreholes, the cross-sectional areas are smaller than those of the drill bits. We do not have an explanation for these phenomena.

Our sonic log data are highly variable, with P-wave velocity estimates varying between 3.6 and 5.1 km/s (column h in Figs. 6 and 7). Intact rock at 30–40 depth in SB50S has an average velocity of ~4.7 km/s and that throughout much of SB50N has a slightly lower average velocity of ~4.5 km/s. Large deviations from these values occur near most intersected fractures in SB50S, but only near N1 and N2 in SB50N.

The general trends in the single-hole radar velocities are not significant; decreasing velocities in the lower parts of SB120 and SB50S (column j in Figs. 5 and 6) correlate with the decreasing borehole cross-sectional areas (column f in Figs. 5 and 6). Notable deviations from the median 0.120 m/ns radar velocity that exceed the estimated inaccuracy of ±0.003 m/ns are recorded near discontinuities A4–A7 and A16 in SB120, S1–S7 and S10 in SB50S and N1–N2 and N7–N9 in SB50N. Most of these velocity deviations are accompanied by amplitude anomalies (column k in Figs. 5–7).

6.2. Crosshole tomogram and VRP velocity–depth models

Radar velocities and attenuations are remarkably uniform in the SB50S–SB50N tomograms of Fig. 11.

Fig. 5. Log and other data acquired in borehole SB120 and information on selected surface fracture zones. a) Televiewer log showing the most important fracture zones (red lines) intersected by the borehole, b) dip azimuths and dips of these fracture zones, c) dip azimuths and dips of correlated surface fracture zones, d) dips of relevant radar reflections, e) estimated minimum lengths of certain fracture zones, f) caliper log (dashed line is the nominal area of the drill bit), g) horizontal displacements/year determined from repeat inclinometer measurements (? indicates uncertain measurements), i) 1-D velocities determined from VRP measurements, j) single-hole radar velocities, k) single-hole radar amplitudes, and l) single-hole radar section highlighting the most important reflections (see Fig. 8). The decreasing borehole cross-sectional area identified in column f) (see also trend of decreasing single-hole radar velocities) is caused by drill-bit abrasion. Borehole elevations and depths are relative to the top of borehole SB50N (2360.4 m above sea level).

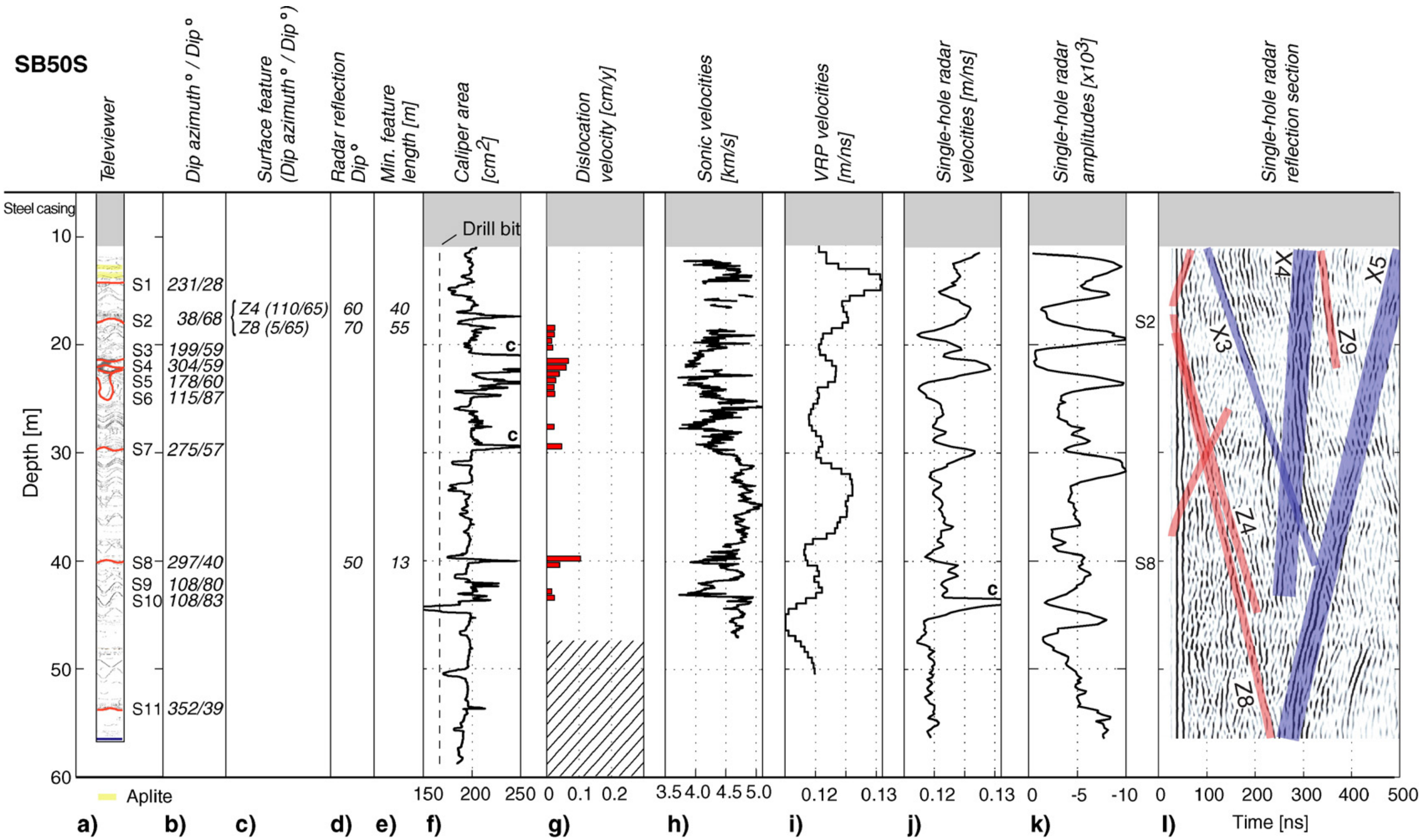

Fig. 6. As for Fig. 5, except for borehole SB50S and the addition of the sonic log in column h). The c's in f) and j) identify clipped values.

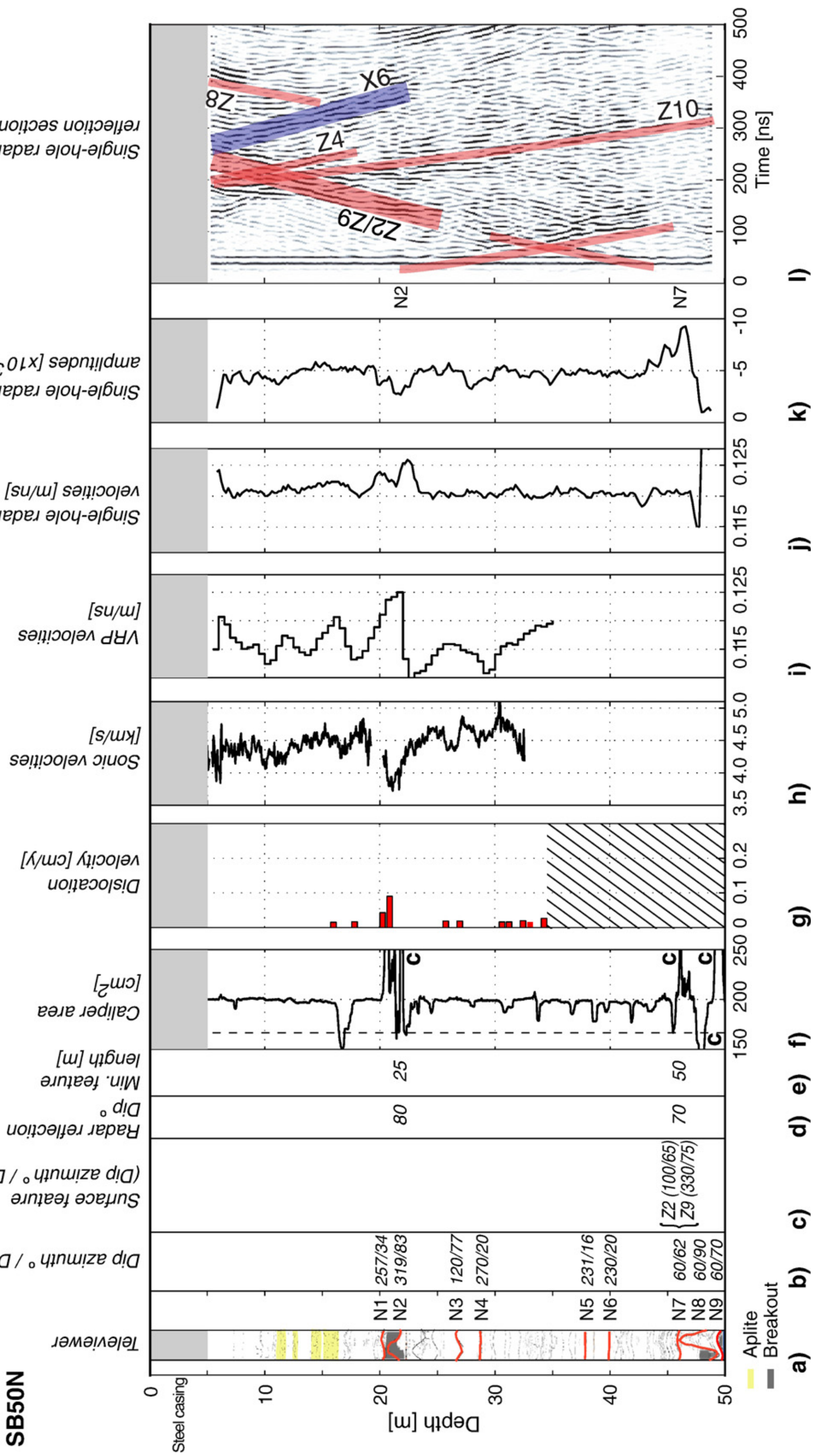

Fig. 7. As for Fig. 6, except for borehole SB50N.

It is for this reason that we represent them in terms of only three ranges of values. More than 80% of the velocities lie between 0.118 and 0.122 m/ns and all values are between 0.114 and 0.126 m/ns (i.e. ±5% variation about the median value of 0.120 m/ns). The trends of the VRP velocity–depth models (column i in Figs. 6 and 7) follow closely the velocities along the edges of the tomograms, with small positive velocity anomalies near SB50S at depths of 11–17 m and 30–38 m and near SB50N at 19–20 m. Attenuations between SB50S and SB50N are mostly between 0.00025 and 0.00035 m^{-1}, with a single noteworthy anomalous zone of 0.00040 m^{-1} near SB50N at 18–21 m depth.

Velocity and attenuation anomalies that intersect SB50N near 20 m depth coincide with spallation zones and displacements at the N1 and N2 discontinuities and associated prominent sonic velocity and single-hole radar velocity and amplitude anomalies. The slight increase in velocity at 11–17 m depth near SB50S occurs close to air-filled fracture zone S1 and the low velocities and coincident high attenuations at 18–19 depth may be explained by the presence of clays and silts in fracture zone S2. There are no explanations from the televiewer log for the small decreases and increases in velocity at other locations near SB50S. There is a hint in the attenuation tomogram that the two shallow dipping discontinuities N1 and S1 are connected.

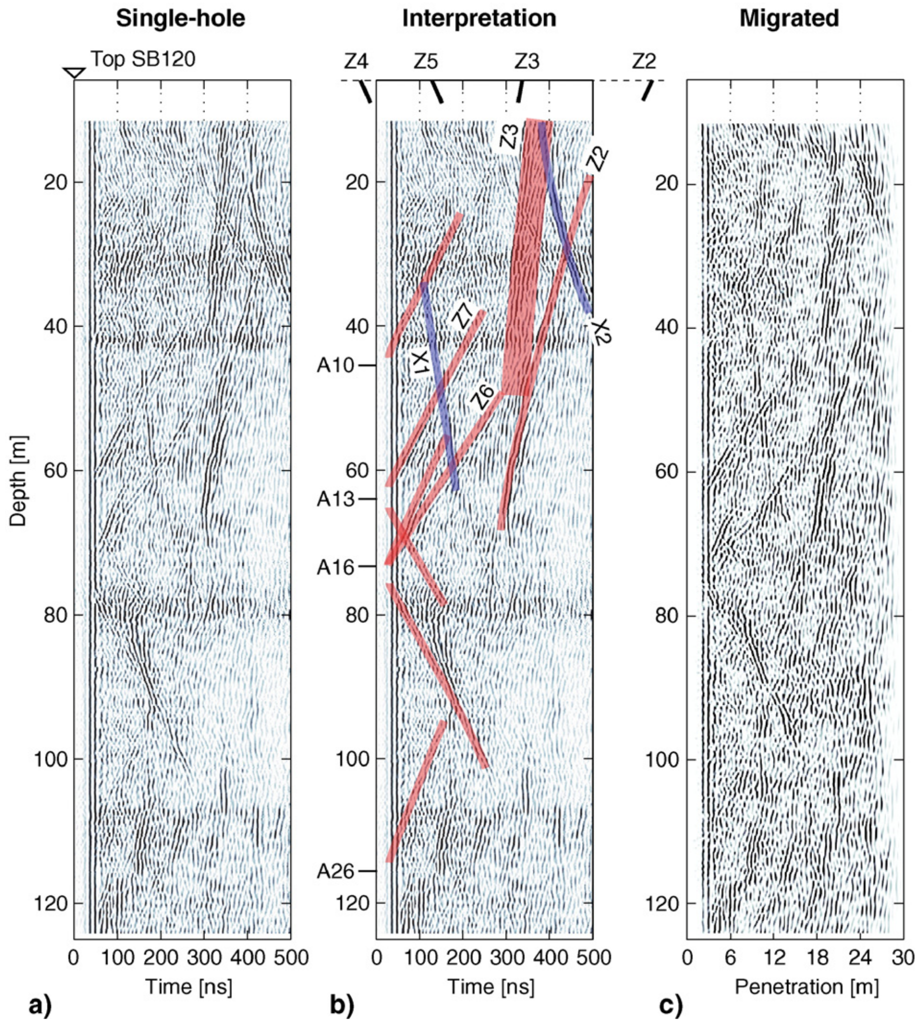

Fig. 8. Processed single-hole radar sections recorded in boreholes a) SB120, d) SB50S and g) SB50N. Interpretations are superimposed on the same three radar sections in b), e) and h). The A's, S's and N's refer to fracture zones intersected by the respective boreholes (Figs. 5–7), the Z's refer to surface fracture zones (Figs. 2a and 3a), and the X's refer to largely unexplained reflections. Phase-shift migrated radar sections are presented in c), f) and i).

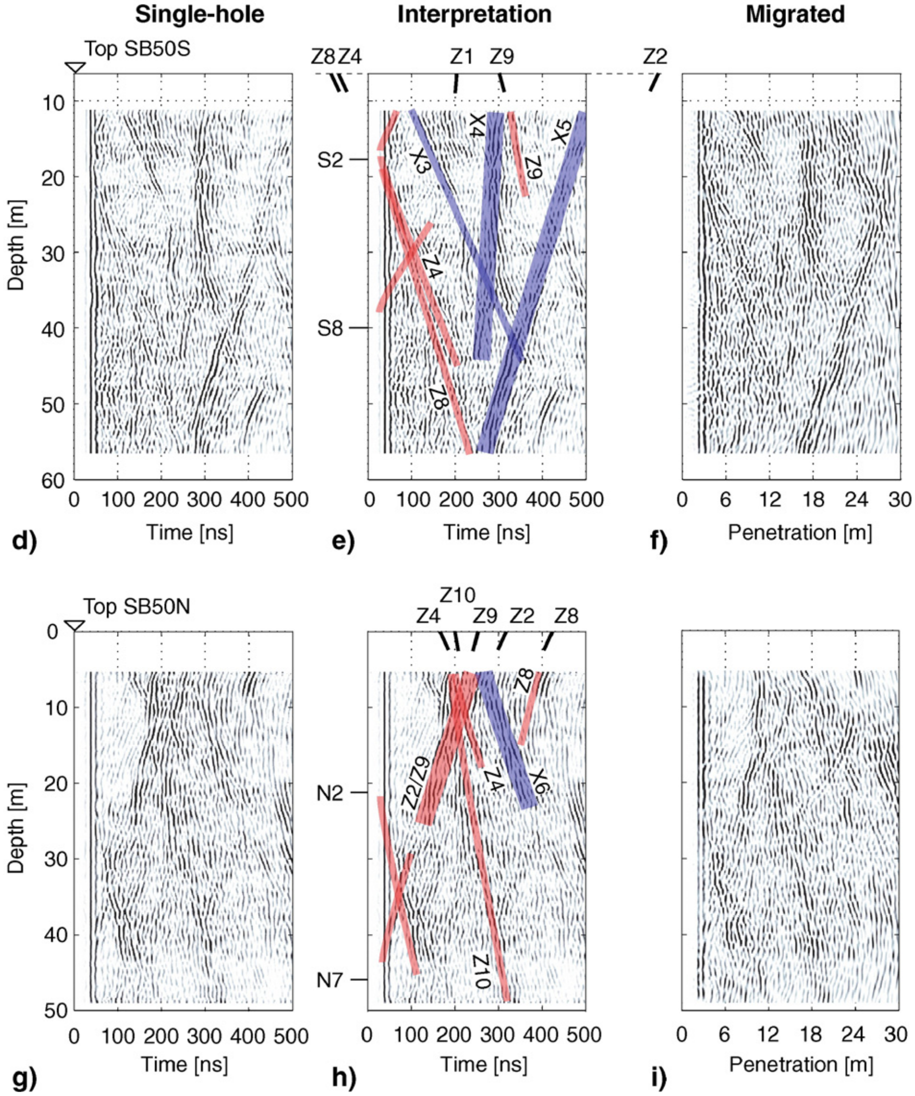

Fig. 8 (*continued*).

Regardless, N1 is the only shallow dipping fracture zone that can be shown to be laterally extensive on the basis of any radar data.

6.3. Single-hole and VRP reflection sections

All three single-hole sections (Fig. 8a, d and g) contain reflections that extend to 500 ns traveltime, indicating the presence of numerous moderately to steeply dipping features within ~30 m of the boreholes. From these sections, we can only define the inclinations of reflectors relative to the boreholes and the depths to those reflectors cut by the boreholes. To locate all reflectors and determine their azimuths requires additional information.

Given that the lithological contacts and foliations of the gneissic rocks are mostly shallow dipping, it is unlikely that geological variations or rock fabrics are the source of reflections in Fig. 8. For the same reason, the shallow-dipping F1 fracture zones and ductile faults can also be eliminated from consideration. From the geological information, it is highly likely that the moderately to steeply dipping F2 and F3 fracture zones are the source of strong reflections. Many are open air-filled structures that have large impedance contrasts relative to the adjacent intact rock. Although the openings of some parts of the F2 and F3 discontinuities may be quite narrow relative to the ~1 m dominant wavelength of our 100 MHz georadar signal, georadar surveying at other locations has shown

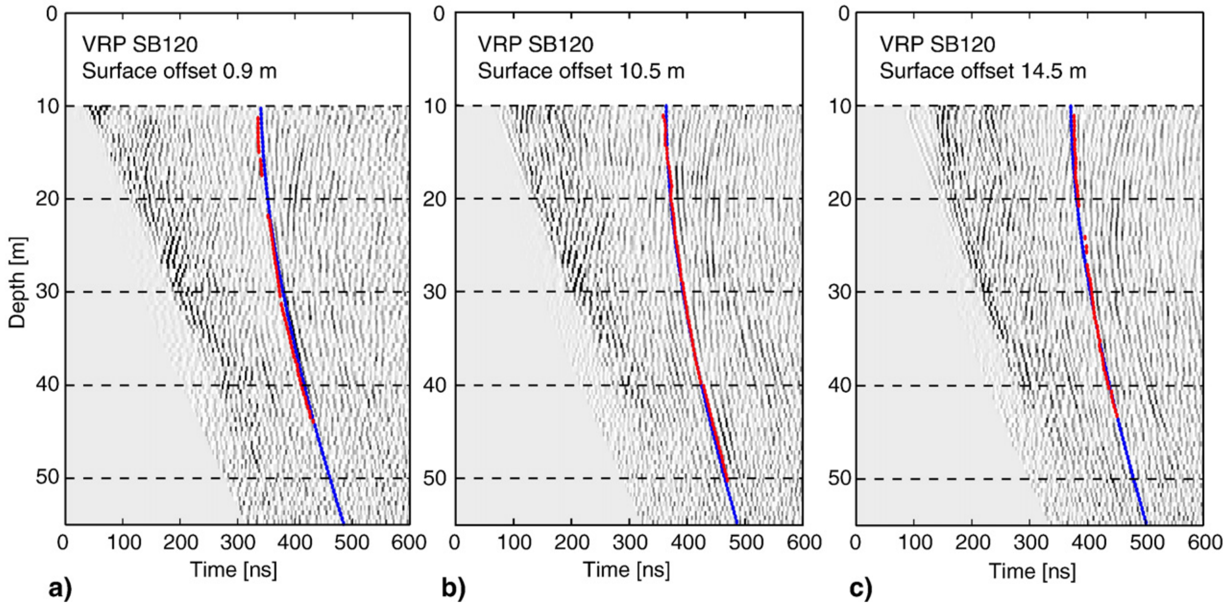

Fig. 9. a)–c): VRP (vertical-radar profile) transmitter gathers for transmitter offsets of 0.9, 10.5 and 14.5 m from borehole SB120 and receivers located between 10.0 m and 57.0 m depth. Red and blue lines are picked reflections and predicted reflections from the best-fit plane shown in Fig. B1 of Appendix B (in places, the lines coincide), respectively.

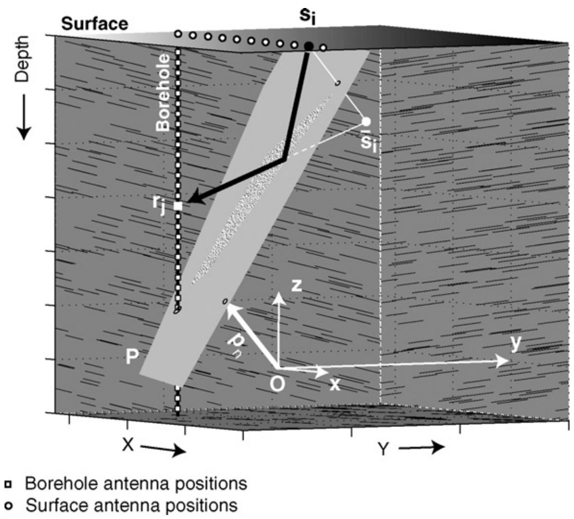

Fig. 10. Sketch illustrating the geometries of an arbitrary planar reflector P defined by the normal vector $\mathbf{p}_n$ and a typical VRP (vertical-radar profile) ray path. Normal vector $\mathbf{p}_n$ can be described by its Cartesian (x, y and z) or radial (l, φ and θ; not shown) coordinates. The least-time ray path of energy travelling from the arbitrary surface source s_i to the arbitrary borehole receiver r_j via reflector P can be constructed with the help of the mirror source $\bar{s}_i$. Reflection points illuminated by rays generated at all positions along the surface profile and recorded at all receiver positions down the borehole are outlined by the speckled pattern on P.

that damage zones around discontinuities in gneissic rock may be sufficiently wide to generate strong reflections (e.g. Grasmueck, 1996).

Our procedure for interpreting the single-hole radar reflections in terms of surface fracture zones F2 and F3 is relatively simple. For a given borehole data set, we begin by linearly extrapolating the significant radar reflections updip until they intersect the horizontal plane containing the borehole collar. Considering the rotational ambiguity of the acquisition geometry, possible intersecting points for each radar reflection describe a circle centred on the borehole collar. We also linearly project the locations of nearby fracture zones on to the same horizontal plane. If the radius of a radar reflection circle is approximately tangent to the projected trace of a fracture zone and the dips of the two features are comparable, we assume that the reflection originates from the depth extension of that fracture zone.

Our interpretations of the various radar reflection zones are presented in Fig. 8b, e and h. Dips and extrapolated positions of the surface fracture zones at the level of the borehole collars are shown along the tops of these figures. They are plotted to the left or right of the borehole axes according to the reflection zones with which they are correlated. Reflection zones that can be related to borehole or surface discontinuities are marked red in Fig. 8b, e and h (also reproduced in column 1 of Figs. 5–7). Other important reflection zones are marked

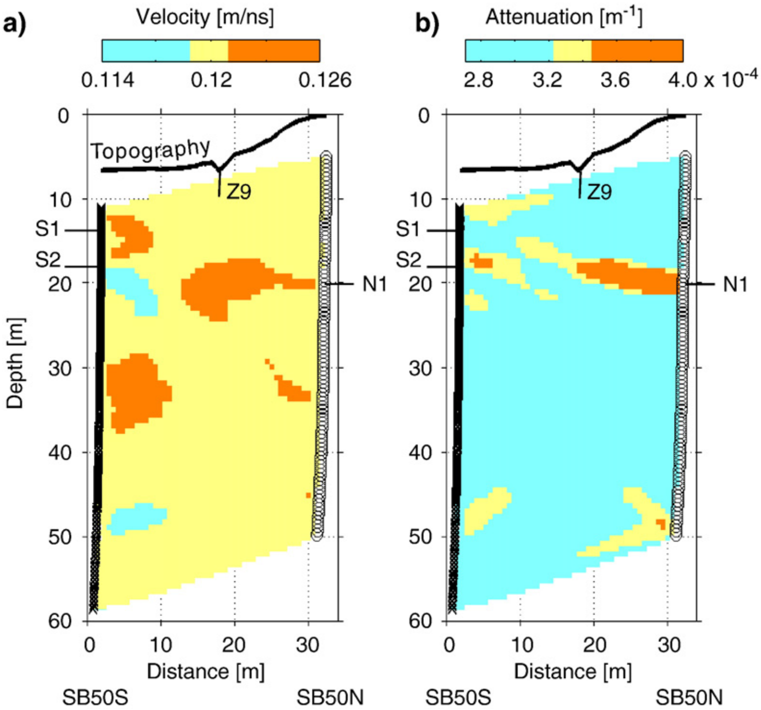

Fig. 11. a) Velocity and b) attenuation tomograms derived from the crosshole georadar data generated in borehole SB50S and recorded in borehole SB50N. S1, S2 and N1 are fracture zones identified in the boreholes.

blue. In Fig. 12, we display the projected surface locations of all significant radar reflectors together with their dips and minimum lengths.

6.4. Fracture zones near SB120

No radar reflections are associated with Z4 and Z5, the two surface fracture zones closest to the collar of SB120 (Figs. 8a–c and 12). Simple linear extrapolation demonstrates that Z4, which is only ~2 m from the collar, and the actively moving borehole fracture A1 are the same discontinuity (note the similarity of their dip azimuths and dips in columns b and c of Fig. 5). Although the discrete reflection X1 projects upwards to the general vicinity of the borehole collar, its very steep dip and lack of projected intersection with the borehole are not compatible with it being a reflection from the Z4–A1 fracture zone. In Fig. 12, we place the surface projection of X1 to the east of SB120. This speculative interpretation assumes that X1 is caused by an F3-type fracture zone that parallels the Z4–A1 and Z5 fracture zones.

Surface fracture zone Z3 is the probable source of (i) a broad band of steeply dipping strong reflections that can be traced to at least 50 m depth on the single-hole radar section (Fig. 8a–c) and (ii) the continuous reflection recorded on the VRP data set (Fig. 9 and Appendix A). The dips and locations of these reflections are consistent with surface observations (Fig. 12). A much thinner band of reflections projects from ~70 m depth to near the expected position of surface fracture zone Z2. A rare steeply dipping event recorded on surface 3-D georadar data (Fig. 13; for the location of the cross-section in Fig. 13 see Fig. 2b) supports our assertion that Z2 is a radar reflector at this location.

Of the twenty-six fracture zones identified along the length of SB120 in Fig. 5, only A10, A13, A16 and A26 generate moderate to strong radar reflections. According to Fig. 8a–c, they dip 53–67° and can be followed over lengths of at least 20–40 m. The 320–350° azimuths indicated by the televiewer logs suggest that they all belong to the F2 fracture system and the repeat inclinometer measurements demonstrate that they are all moving. Only A16 has an associated spallation zone and a significant single-borehole radar velocity anomaly. None of these reflection zones can be traced beyond a sequence of prominent steeply dipping reflections starting at ~300 ns traveltime. Nevertheless, it is noteworthy that the A13 and A16 fracture zones and reflections project southwestwards to where Z7 and Z6 are observed at the surface.

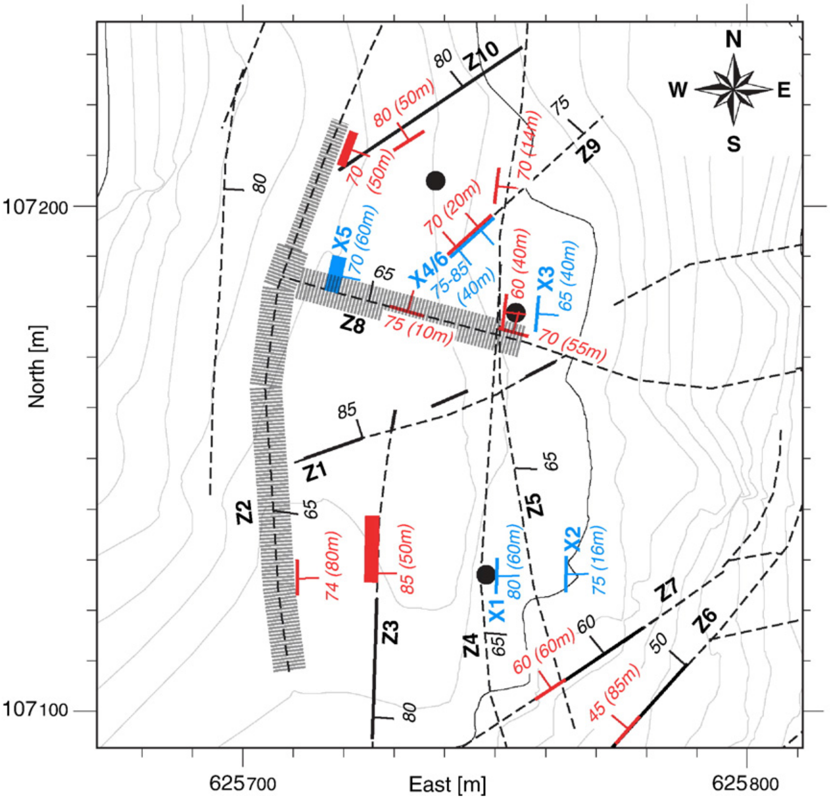

Fig. 12. Projected surface positions of the most significant radar reflectors (from Figs. 8 and 9) plotted on a simplified version of Fig. 2b. Thicknesses of the red and blue lines correspond approximately to the reflection zone thicknesses. The surface locations of the X1–X6 reflectors (blue lines) are highly speculative; they have been chosen to be consistent with the orientations of the F2 and F3 systems of fractures.

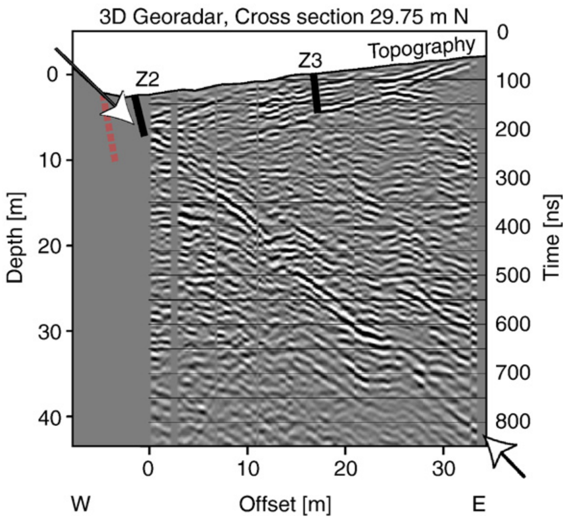

Fig. 13. Non-migrated cross-section extracted from a 3-D surface georadar data set that samples a large volume of rock between SB120 and the extrapolated location of the Z2 fracture zone (for details on the acquisition and processing of these data see Heincke et al., 2005). The very steep (>70°) reflection highlighted by the arrows would approximately migrate to the dashed position shown at the surface. It corresponds closely to the Z2 reflection identified in Fig. 8b.

Furthermore, the orientations of A13 and A16 are similar to those of Z7 and Z6, respectively (see columns b and c in Fig. 5). If this correlation is correct, then the Z7–A13 and Z6–A16 fracture zones extend ~60 and ~85 m from their borehole intersections to the surface, respectively.

We cannot correlate any surface feature with the X2 band of radar reflections, despite its proximity to the surface (Fig. 8a–c). Considering its strength, continuity, length (16 m) and steep dip (75°), we infer that X2 is generated at a fracture zone. Although it is shown as an F3-type fracture zone that parallels the neighbouring A1–Z4 and Z5 fracture zones in Fig. 12, it could also be an F2-type fracture zone that lies to the north of the borehole.

6.5. Fracture zones near SB50S

Surface fracture zones Z4 and Z8 and two linear radar reflections with slightly different dips project to the general vicinity of the fracture zone S2 in borehole SB50S (Fig. 8d–f). Both surface fracture zones pass to within 5 m of the borehole collar (Fig. 12). The dips of the surface and borehole fracture zones are similar to those of the radar reflections (columns b, c and d in Fig. 6) and although the dip azimuths of the fractures differ somewhat, S2 is a complex zone with substantial spalling (column f in Fig. 6) that could indeed represent the effects of intersecting fractures with different orientations. Our interpretation implies that the Z4–S2 and Z8–S2 fracture zones have minimum subsurface lengths of ~40 and ~55 m, respectively.

Reflections from the large open surface fracture zone Z9 that bisects borehole SB50S and SB50N (Fig. 12) are best observed on the migrated section of Fig. 8f. They can be traced dipping ~70° over a length of ~20 m. Even though the equally important surface fracture zone Z1 is not the source of near-surface reflections, a near-vertical reflection at 27–38 m depth could originate from its depth extension.

A rather weak radar reflection may be associated with borehole fracture zone S8 (Fig. 8e), which has a localized spallation zone and is moving. It is noteworthy that there are no clear reflections from the S3–S5, S7, S9 and S10 fracture zones, many of which have caliper, displacement and/or single-hole radar velocity and amplitude anomalies.

The three prominent steeply dipping (65–85°) reflection zones X3–X5 (Fig. 8d–f) do not correlate with mapped surface discontinuities, despite their 40–60 m lengths and proximity to the surface. Considering the geology near SB50S, X3 could originate from a buried fracture zone that either lies to the east of the borehole and parallels Z4 (as shown in Fig. 12) or lies to the north and parallels Z8. A southeast origin for X4 (i.e. a fracture zone parallel to and southeast of Z1) seems unlikely, because outcrop is extensive at that location. A possible explanation for X4 is provided in the next section. A buried F3-type fracture zone located a few metres to the east of surface fracture zone Z2 could explain the deep-penetrating X5 band of reflections (Fig. 12).

6.6. Fracture zones near SB50N

Four surface fracture zones Z2, Z4, Z9 and Z10 lie within 10–20 m of the SB50N collar. Interference of reflections from these structures creates a complicated reflection pattern between 100 and 300 ns on the SB50N radar sections (Fig. 8g–h). Fracture zone Z10 is the probable source of the steeply dipping (80°) reflections that can be followed for >50 m from near the surface to the base of the radar section. A broad ~70° dipping band of reflections that could originate from Z2 and/or Z9 projects down towards reflections from the region of borehole fracture N7, where large caliper and single-hole velocity and amplitude anomalies are recorded. The dips of the reflection band and the surface and borehole fracture zones are similar, but the dip azimuths of the fracture zones differ (columns b, c and d in Fig. 7). Surface fracture Z4 correlates well with a rather distinct 70° dipping reflection fabric that cross-cuts the interpreted Z2, Z9 and Z10 reflection zones over a length of ~14 m, whereas Z8 may be related to some curvilinear events that approach the surface.

Borehole discontinuities N1 and N2 generate substantial caliper, displacement, sonic velocity, radar velocity and radar amplitude anomalies and are the primary active discontinuities intersected by the borehole (columns f–k in Fig. 7). We have already noted that the shallow-dipping N1 discontinuity is also the source of velocity and attenuation anomalies on the tomograms of Fig. 11. By comparison, the steeply dipping N2 fracture zone produces strong reflections that dip 80° over a distance of ~25 m on the single-hole radar section of Fig. 8g–i.

Finally, we note that reflection zones X4 and X6 on the SB50S and SB50N radar sections (Fig. 8d–i), respectively, could originate from the same fracture zone. Their dips, distances from the boreholes and similarity of reflection character are consistent with a common reflector that coincides with the surface location of Z9. If this interpretation is correct, then Z9 is actually the junction of two distinct fracture zones. The first fracture zone is open at the surface and dips steeply to the northwest (Z9 in Fig. 8d–i). It is a member of the F2 system of fractures. The second fracture zone, which is equally or more important in terms of the strength and continuity of radar reflections, dips very steeply to the southeast.

7. Discussion and conclusions

Of the three georadar methods tested, the VRP and crosshole techniques provided only limited useful information at the Randa study site. Velocities determined from the VRP data had disappointingly low resolutions, and only a single interpretable reflection was observed on the VRP source and receiver gathers (Fig. 9). The crosshole tomograms provided valuable median radar velocity and attenuation estimates, but they were surprisingly featureless (Fig. 11). Only three low contrast anomalies could be related to discontinuities that intersected the boreholes. The most significant of these anomalies suggested that the shallow-dipping N1 discontinuity extended >20 m from SB50N. The absence of velocity and/or attenuation anomalies in the region of the steeply dipping surface fracture zone Z9 (and possibly also X4/X6), which crossed the tomographic plane, was likely due to the insensitivity of the crosshole radar method to narrow borehole-parallel structures.

Single-hole radar reflections appear to have been generated at surface facture zones Z2–Z4 and Z6–Z10 and at borehole fracture zones A10, A13, A16, A26, S2, S8, N2 and N7. Based on our interpretations of the radar data and the fracture zone orientations measured at the surface and within the boreholes, we proposed the following connections: Z2–N7, Z4–S2, Z6–A16, Z7–A13, Z8–S2 and Z9–N7. In addition, simple linear extrapolation demonstrated that surface fracture zone Z4 and nearby borehole fracture zone A1 were the same discontinuity.

We note that the minimum depth dimensions of nearly all fracture zones are large fractions of their mapped lateral dimensions. Consequently, we infer that the majority of important surface fracture zones extend deep into the mountain slope.

Since many borehole fracture zones were not the source of strong borehole geophysical anomalies (Figs. 5–7) and, as such, were likely to be local features, the lack of associated radar reflections was not surprising. However, there were no obvious explanations for the absence of radar reflections from borehole fracture zones A4, A5, A7 and S4–S7, all of which had caliper, displacement, radar velocity and radar amplitude anomalies, and from surface fracture zones Z1 and Z5. In contrast, there was no surface or borehole evidence for the origins of the six prominent reflection bands X1–X6 (Fig. 8). We suggested that they were generated at five unmapped fracture zones, four of which could be traced to within 5 m of the surface.

A 3-D model that shows the approximate sizes and geometries of many fracture zones observed at the surface, in the boreholes and in the interpreted georadar data is presented in Fig. 14. In constructing this model, the depth limits estimated from the VRP and single-hole radar data are assumed to apply to the entire lengths of the fracture zones. Except for the newly discovered X4/

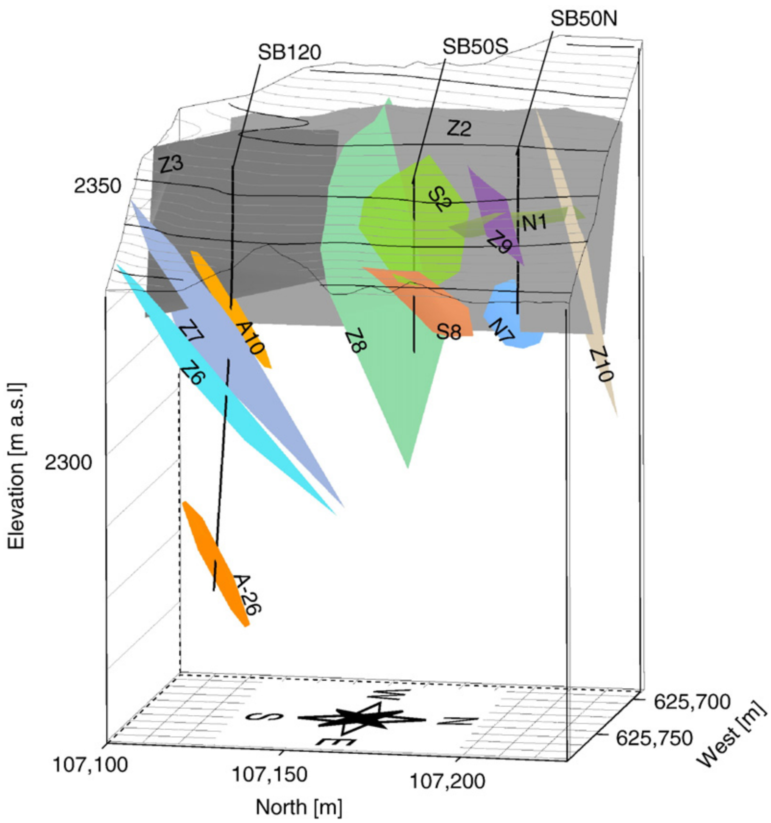

Fig. 14. Perspective view of major fracture zones identified in the single-hole radar data. The locations of most fracture zones are constrained by surface and borehole observations. Fracture zone Z4 has been omitted, because it would obscure the other fractures when the rock mass is viewed from this direction.

X6 structure, all fracture zones can be assigned to one of the F1–F3 systems of fractures. If X4 on the SB50S radar section is indeed the same as X6 on the SB50N radar section, then this would be the first example of a slightly southeasterly dipping fracture zone.

Fig. 14 suggests that the investigated rock volume is divided by major fracture zones into a number of discrete blocks of varying sizes. From our new data, it is not possible to delineate a master fault that could control any future rockslide. However, we have demonstrated that Z2 and Z10, the two furthest investigated fracture zones from the 1991 rock scarp, are major structures that extend at least 50 m beneath the surface. Consequently, they likely define the minimum northwesterly extent of potentially unstable rock (Fig. 2a).

Acknowledgements

We thank Simon Loew and Erik Eberhardt for their cooperation in this interdisciplinary project and appreciate the very helpful suggestions provided by Heinrich Horstmeyer. The comments by two journal reviewers are greatly appreciated. The optical televiewer logs and the inclinometer surveys were performed by Terratec GmbH (Germany) and Stump Foratec AG (Switzerland), respectively. We are grateful to Jean Daniel-Rouiller from CREALP (Research Centre on Alpine Environment, Switzerland) for providing the digital terrain model and geodetic survey data, and to the local authorities of Randa for providing logistical support. This project was funded by the Swiss National Science Foundation (Project No. 2000-066877).

Appendix A. Synthetic examples

To illustrate the benefits and limitations of our grid search technique for locating planar boundaries that are the source of reflections in VRP data, four synthetic examples are presented in Fig. A1. A boundary is uniquely defined by a vector $\mathbf{p}_n = [l, \varphi, \theta]$ that is normal

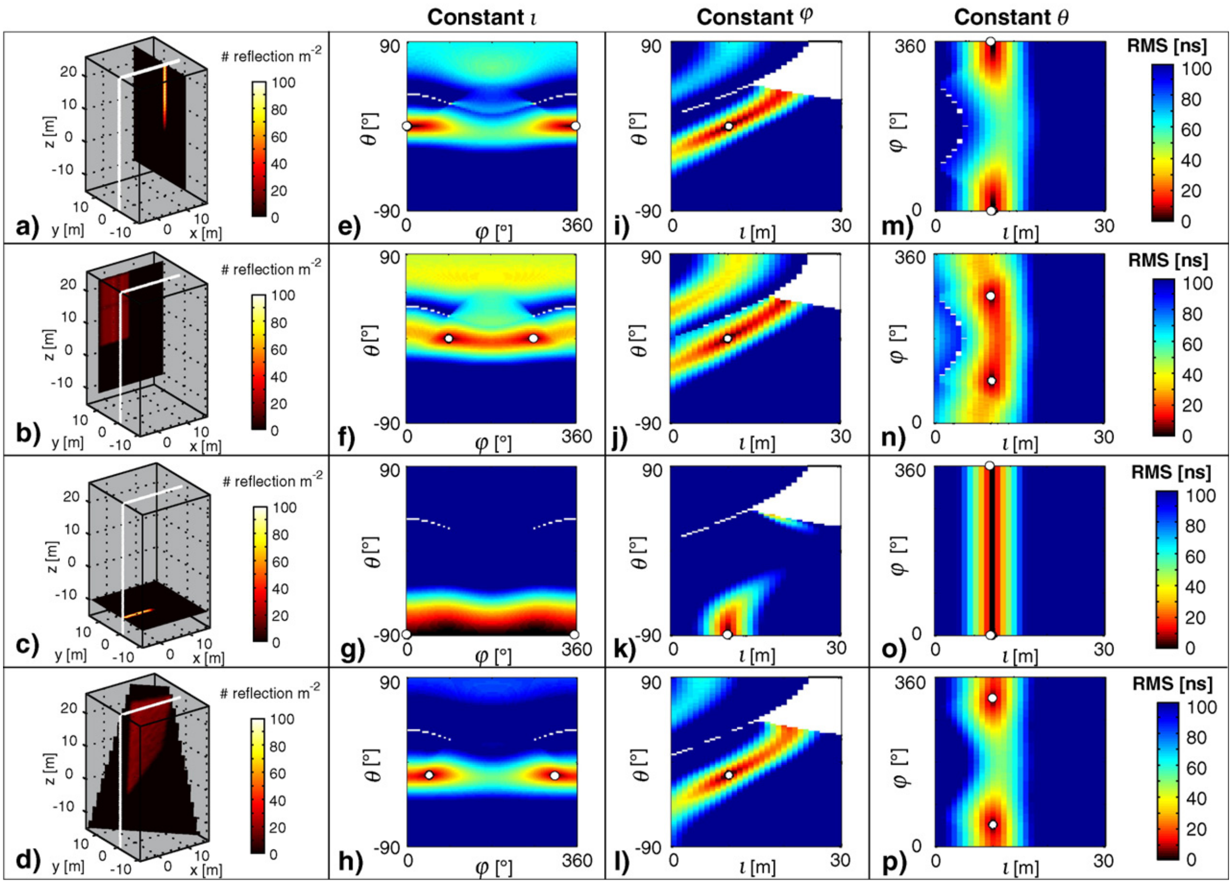

Fig. A1. Results of tests on synthetic data. a)–d): Position for four planes (black areas) with respect to the source–receiver arrays (white lines). Colours on the planes represent reflection point densities. e)–h): RMS slices for constant true normal vector lengths 1. i)–l): RMS slices for constant true azimuths φ. m)–p): RMS slices for true dips θ. Correct solutions are represented by the white dots in panel e) to p).

to the plane, where l, φ and θ are spherical coordinates relative to an arbitrary origin. The first column of Fig. A1 shows the models and numbers of reflections per square metre for the fixed transmitter–receiver geometry identified by the white lines. The second to fourth columns show slices extracted from the volume of root–mean square (RMS) differences between true and predicted reflection traveltimes based on all possible trial planar boundaries. They show RMS differences for varying φ and θ with l fixed to the correct value (second column), varying l and θ with φ fixed to the correct value (third column), and varying l and φ with θ fixed to

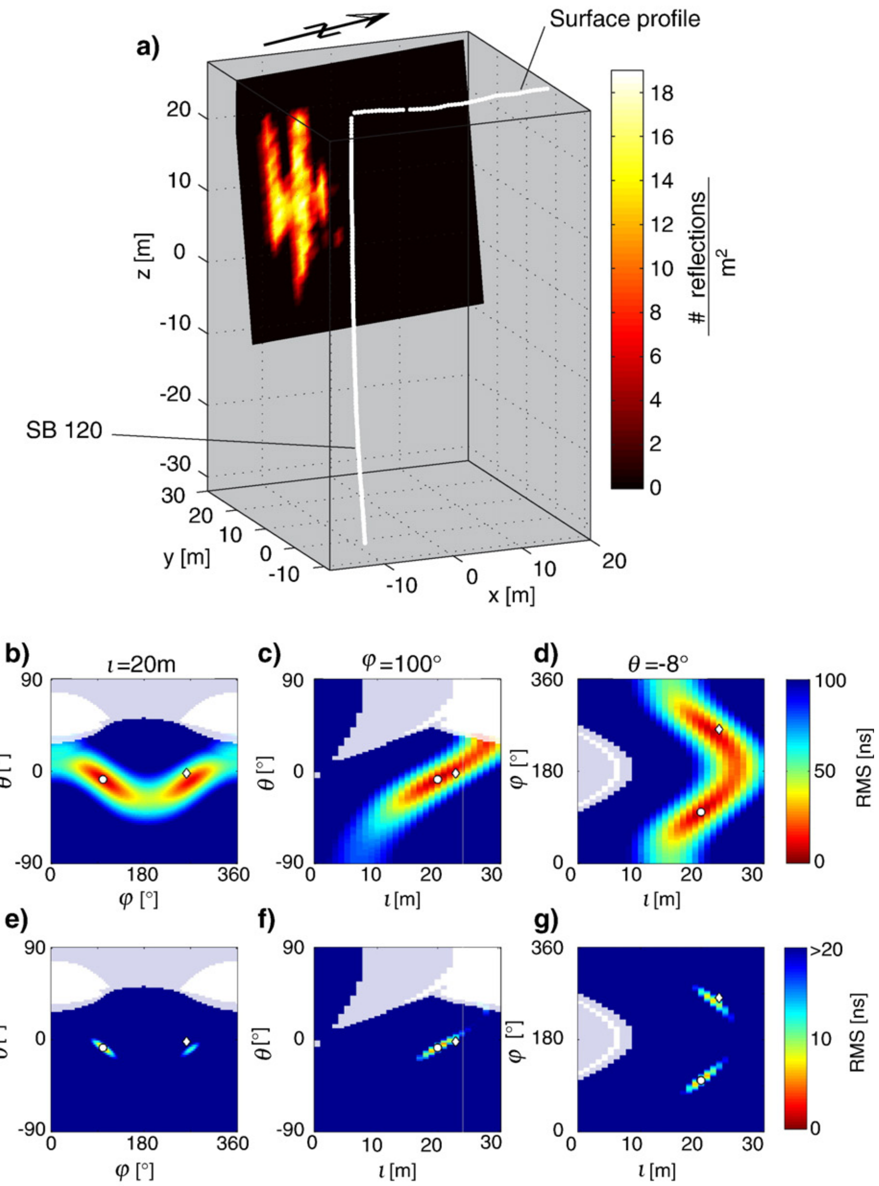

Fig. B1. Results of vertical-radar profile (VRP) grid search based on data recorded in borehole SB120. a) Geometry of sources and receivers (white lines and white dots) and best fitting plane (black area) shown with its reflection point density. b)–d): RMS slices for best fitting 1, φ and θ; colour saturation is proportional to the number of data points considered for the RMS calculation (e.g. white delineates areas not sampled and light blue shows regions poorly sampled). the projections of the two symmetric best fitting solutions $\mathbf{p}_n^{\mathbf{best\_1}}$ and $\mathbf{p}_n^{\mathbf{best\_2}}$ are marked with a white circle and diamond, respectively. e)–g): As for b)–d), but with limited colour scale (i.e. all values with RMS values >20 are blue).

the correct value (fourth column). The minima of the RMS differences are identified by small white dots. Blank regions represent areas of the RMS slices for which there are no reflection points.

For the vertical plane defined by the normal vector $\mathbf{p}_n$=[10, 0, 0], all reflection points occur along a vertical strip (Fig. A1a). The RMS slices in the top row indicate that the parameters defining the normal vector are well resolved, with the only potential for a minor trade-off being between l and θ (Fig. A1i). There is a similar potential for a minor trade-off between l and θ for a vertical plane that parallels the acquisition plane containing the sources and receivers (Fig. A1b and j). For this plane, defined by the normal vector $\mathbf{p}_n$=[10, 90, 0], there are two equivalent solutions at φ=90 and 270° (Fig. A1f and n). With the exception of vertical planes perpendicular to the acquisition plane (e.g. Fig. A1a), there always exists at least two solutions, one to the "left" and one to the "right" of the data acquisition plane.

The horizontal plane in Fig. A1c mimics a common situation in VSP studies (Hardage, 1983; Dillon and Thomson, 1984). Since the normal vector $\mathbf{p}_n$=[10, 0, 90] to the plane is vertical, φ is not relevant, but correct values of l and θ are reconstructed accurately (Fig. A1k). Finally, the RMS slices in the bottom row are the results for an arbitrary plane defined by the normal vector $\mathbf{p}_n$= [10, 46, −14]. These results, including the trade-offs and ambiguities, are similar to those shown for the vertical planes in the upper two rows.

Information contained in Fig. A1 demonstrates that it is possible to retrieve the locations and orientations of most reflecting planes from high quality VRP data. Reasonable estimates of the uncertainties of these parameters can be determined from the isosurface of RMS differences corresponding to the picking accuracy of the reflection times. The left–right ambiguity is best resolved by considering other geological and/or geophysical information.

Appendix B. Field examples

The results of applying the grid search algorithm to the reflection traveltimes picked from SB120 VRP data are shown in Fig. B1. We use a constant velocity of 0.12 m/ns and set the origin of the coordinate system to the centre of the source–receiver array to provide trial vectors that uniformly sample the volume of interest. To display the minimum RMS values, we choose RMS slices (Fig. B1b–d) defined by l, φ and θ values that are equal to our preferred solution (Fig. B1a). The two well determined minima in Fig. B1b–d correspond to normal vectors $\mathbf{p}_n^{\mathbf{best\_1}}$=[20 m, 100°, −8°] and $\mathbf{p}_n^{\mathbf{best\_2}}$=[23 m, 262°, 2°]. The RMS differences at both minima are in the 3–4 ns range, well below the estimated 5 ns picking uncertainty of the reflection traveltimes. To determine plausible uncertainties for each parameter, we re-scale the RMS colour scale in Fig. B1e–g to lie between 0 and 20 ns, such that all values >20 ns are uniformly dark blue. This figure demonstrates that a 5 ns uncertainty in reflection traveltime picking corresponds approximately to parameter uncertainties of Δl=±2 m, $\Delta\varphi$=±16° and $\Delta\theta$=±7°.

The asymmetry of the two solutions in Fig. B1 is a result of the borehole curvature. Predicted traveltimes based on these solutions are shown by the blue lines superimposed on the observed data in Fig. 9. They match well the traveltimes of the identified reflections. The projected surface location of the plane defined by $\mathbf{p}_n^{\mathbf{best\_1}}$ would be 23.6±1.0 m from SB120 with a 86±8° dip azimuth and 82±4° dip, whereas that defined by $\mathbf{p}_n^{\mathrm{best\_2}}$ would occur at a distance of 22.0±1.0 m from the borehole with a 284±8° dip azimuth and 88±4° dip.

References

Bader, S., Kunz, P., 2000. Climate Risks — The Challenge for Alpine Regions, Final Scientific Report NRP 31. vdf Hochschulverlag, Zürich.

Bruno, F., Marillier, F., 2000. Test of high-resolution seismic reflection and other geophysical techniques on the Boup landslide in the Swiss Alps. Surveys in Geophysics 21, 335–350.

Cooke, R.U., Doornkamp, J.C., 1990. Geomorphology in Environmental Management: A New Introduction. Clarendon Press, Oxford.

Cummings, D., 2000. Transient electromagnetic survey of a landslide and fault, Santa Susanna Mountains, Southern California. Environmental and Engineering Geosciences 6, 247–254.

Dillon, P.B., Thomson, R.C., 1984. Offset source VSP surveys and their image reconstruction. Geophysical Prospecting 32, 790–811.

Dussauge-Peisser, C., Wathelet, M., Jongmans, D., Hantz, D., Couturier, B., Sintes, M., 2003. Investigation of a fractured limestone cliff (Chartreuse Massif, France) using seismic tomography and ground-penetrating radar. Near Surface Geophysics 1, 161–170.

Eberhardt, E., Willenberg, H., Loew, S., Maurer, H.R., 2001. Active rockslides in Switzerland — understanding mechanisms and processes. International Conference on Landslides — Causes, Impacts and Countermeasures, Davos, pp. 25–34.

Engheta, N., Papas, C.H., Elachi, C., 1982. Radiation patterns of interfacial dipole antennas. Radio Science 17, 1557–1566.

Erismann, T.H., Abele, G., 2001. Dynamics of Rockslides and Rockfalls. Springer, Berlin.

Glade, T., Anderson, M., Crozier, M.J., 2005. Landslide Hazard and Risk. John Wiley & Sons.

Grasmueck, M., 1996. 3-D ground-penetrating radar applied to fracture imaging in gneiss. Geophysics 61, 1050–1064.

Hack, R., 2000. Geophysics for slope stability. Surveys in Geophysics 21, 423–448.

Hardage, B.A., 1983. Vertical Seismic Profiling, Part A, Principles. Geophysical Press, London.

Havenith, H.-B., Jongmans, D., Abdrakhmatov, K., Trefois, P., Delvaux, D., Torgoev, I.A., 2000. Geophysical investigations of seismically induced surface effects: case study of a landslide in the Suusamyr valley, Kyrgyzstan. Surveys in Geophysics 21, 351–370.

Heincke, B., van der Kruk, J., Green, A.G., Horstmeyer, H., 2005. Acquisition and processing strategies for 3-D georadar surveying a region characterized by rugged topography. Geophysics 70, K53–K61.

Heincke, B., Green, A.G., van der Kruk, J., Willenberg, H., 2006. Semblance-based topographic migration (SBTM): a method for identifying fracture zones in 3-D georadar data. Near Surface Geophysics 4, 79–88.

Heincke, B., Maurer, H.R., Green, A.G., Willenberg, H., Burlini, L., Spillmann, T., in press. Characterizing an unstable mountain slope using shallow 2-and 3-D seismic tomography. Geophysics.

Holliger, K., Musil, M., Maurer, H.R., 2001. Ray-based amplitude tomography for crosshole georadar data: a numerical assessment. Journal of Applied Geophysics 47, 285–298.

Husen, S., Kissling, E., 2001. Local earthquake tomography between rays and waves: fat ray tomography. Physics of the Earth and Planetary Interiors 123, 127–147.

Jaboyedoff, M., Ornstein, P., Rouiller, J.-D., 2004. Design of a geodetic database and associated tools for monitoring rock-slope movements: the example of the top of Randa rockfall scarp. Natural Hazards and Earth System Sciences 204, 187–196.

Jongmans, D., Hemroulle, P., Demanet, F., Renardy, F., Vanbrabant, Y., 2000. Application of 2-D electrical and seismic tomography techniques for investigating landslides. European Journal of Environmental and Engineering Geophysics 5, 75–89.

Maurer, H.R., 1996. Systematic errors in seismic crosshole data: application of the coupled inverse technique. Geophysical Research Letters 23, 2681–2684.

McCann, D.M., Forster, A., 1990. Reconnaissance geophysical methods in landslide investigations. Engineering Geology 29, 59–78.

Menke, W., 1984. The resolving power of cross-borehole tomography. Geophysical Research Letters 11, 105–108.

Musil, M., Maurer, H.R., Holliger, K., Green, A.G., 2006. Internal structure of an Alpine rock glacier based on crosshole georadar traveltimes and amplitudes. Geophysical Prospecting 54, 273–285.

Olsson, O., Falk, L., Forslund, O., Lundmark, L., Sandberg, E., 1992. Borehole radar applied to the characterization of hydraulically conductive fracture zones in crystalline rock. Geophysical Prospecting 40, 109–142.

Podvin, P., Lecomte, I., 1991. Finite difference computation of traveltimes in very contrasted velocity models: a massively parallel approach and its associated tools. Geophysical Journal International 105, 271–284.

Rector III, J.W., Washbourne, J.K., 1994. Characterization of resolution and uniqueness in crosswell direct-arrival traveltime tomography using the Fourier projection slice theorem. Geophysics 59, 1642–1649.

Sartori, M., Baillifard, F., Jaboyedoff, M., Rouiller, J.-D., 2003. Kinematics of the 1991 Randa rockslides (Valais, Switzerland). Natural Hazards and Earth System Sciences 3, 423–433.

Schindler, C., Cuénod, Y., Eisenlohr, T., Joris, C.-L., 1993. Die Ereignisse vom 18. April und 9. Mai 1991 bei Randa (VS) — ein atypischer Bergsturz in Raten (The April 18 and May 9 events near Randa — an atypical sequential rockfall). Eclogae Geologicae Helvetiae 86, 643–665.

Schmutz, M., Albouy, Y., Guérin, R., Maquaire, O., Vassal, J., Schott, J.-J., Descloîtres, M., 2000. Joint electrical and time domain electromagnetism (TDEM) data inversion applied to the Super Sauze earthflow (France). Surveys in Geophysics 21, 371–390.

Seol, S.J., Kim, J.-H., Cho, S.-J., Chung, S.-H., 2004. A radar survey at a granite quarry to delineate fractures and estimate fracture density. Journal of Environmental and Engineering Geophysics 9, 53–62.

Tronicke, J., Knoll, M.D., 2005. Vertical radar profiling: influence of survey geometry on first-arrival traveltimes and amplitudes. Journal of Applied Geophysics 57, 179–191.

Wänstedt, S., Carlsten, S., Tirén, S., 2000. Borehole radar measurements aid structure geological interpretations. Journal of Applied Geophysics 43, 227–237.

Washbourne, J.K., Rector, J.W., Bube, K.P., 2002. Crosswell traveltime tomography in three dimensions. Geophysics 67, 853–871.

Willenberg, H., 2004. Geologic and kinematic model of a landslide in crystalline rock (Randa, Switzerland). Unpublished Ph.D.thesis, Swiss Federal Institute of Technology, Zürich.

Willenberg, H., Evans, K.F., Eberhardt, E., Loew, S., Spillmann, T., Maurer, H.R., 2004. Geological, geophysical and geotechnical investigations into the internal structure and kinematics of an unstable, complex sliding mass in crystalline rock. Proceedings of the 9th International Symposium on Landslides, Rio de Janeiro.

Zhou, H., Sato, M., 2000. Application of vertical radar profiling technique to Sendai Castle. Geophysics 65, 533–539.